Journal of the Mechanics and Physics of Solids 96 (2016) 411–427

Contents lists available at ScienceDirect

Journal of the Mechanics and Physics of Solids

journal homepage: www.elsevier.com/locate/jmps

Dwell fatigue in two Ti alloys: An integrated crystal plasticity and discrete dislocation study

Zebang Zheng [a,*], Daniel S. Balint [b], Fionn P.E. Dunne [a,b]

[a] Department of Materials, Imperial College London, London SW7 2AZ, United Kingdom
[b] Department of Mechanical Engineering, Imperial College London, London SW7 2AZ, United Kingdom

ARTICLE INFO

Article history:
Received 5 April 2016
Received in revised form
21 June 2016
Accepted 12 August 2016
Available online 21 August 2016

Keywords:
Discrete dislocation plasticity
Dwell fatigue
Load shedding
HCP crystals
Nano-indentation

ABSTRACT

It is a well known and important problem in the aircraft engine industry that alloy Ti-6242 shows a significant reduction in fatigue life, termed dwell debit, if a stress dwell is included in the fatigue cycle, whereas Ti-6246 does not; the mechanistic explanation for the differing dwell debit of these alloys has remained elusive for decades. In this work, crystal plasticity modelling has been utilised to extract the thermal activation energies for pinned dislocation escape for both Ti alloys based on independent experimental data. This then allows the markedly different cold creep responses of the two alloys to be captured accurately and demonstrates why the observed near-identical rate sensitivity under non-dwell loading is entirely consistent with the dwell behaviour. The activation energies determined are then utilised within a recently developed thermally-activated discrete dislocation plasticity model to predict the strain rate sensitivities of the two alloys associated with nano-indentation into basal and prism planes. It is shown that Ti-6242 experiences a strong crystallographic orientation-dependent rate sensitivity while Ti-6246 does not which is shown to agree with recently published independent measurements; the dependence of rate sensitivity on indentation slip plane is also well captured. The thermally-activated discrete dislocation plasticity model shows that the incorporation of a stress dwell in fatigue loading leads to remarkable stress redistribution from soft to hard grains in the classical cold dwell fatigue rogue grain combination in alloy Ti-6242, but that no such load shedding occurs in alloy Ti-6246. The key property controlling the behaviour is the time constant of the thermal activation process relative to that of the loading. This work provides the first mechanistic basis to explain why alloy Ti-6242 shows a dwell debit but Ti-6246 does not.

1. Introduction

Titanium alloys are widely used in gas turbine engines, often under extremes of loading; components include discs and blades. They are utilised widely in the aerospace industry due to their low density, excellent corrosion resistance and high fatigue strength (Lütjering and Williams, 2003; Williams and Starke Jr, 2003). However, it has been well recognised for over 40 years that titanium alloys suffer from cold dwell fatigue often characterised by basal facet nucleation and subsequent growth. The life time reduction resulting from the inclusion of load holds at maximum stress during each loading (e.g. flight)

* Corresponding author.
E-mail address: zebang.zheng12@imperial.ac.uk (Z. Zheng).

http://dx.doi.org/10.1016/j.jmps.2016.08.008
0022-5096/

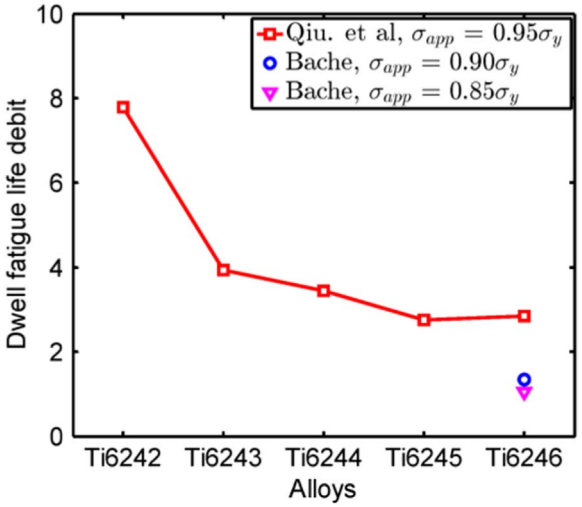

Fig. 1. Dwell debit in Ti-624*x* alloys. (Bache, 2003; Qiu et al., 2014) The dwell fatigue life debit is defined as the fatigue life of low-cycle fatigue divided by that of low-cycle dwell fatigue loading.

cycle is termed the dwell fatigue life debit. It continues to be a significant industrial concern because the associated non-destructive evaluation management is hugely costly, and it remains a safety-critical issue. For example, recent work by Pilchak (Pilchak, 2013) has shown that once nucleated, facet growth rates are more than one order of magnitude faster than (non-dwell) striation growth. Early and more recent experimental evidence (Bache, 2003; Qiu et al., 2014) interestingly shows that the dwell debit in the Ti–6Al–2Sn–4Zr–*x*Mo ($x=2$–6) alloys decreases significantly with increasing Mo content and with decreasing peak stress, as shown in Fig. 1, to the extent that alloy Ti-6242 suffers dwell fatigue whereas alloy Ti-6246 does not. Although significant progress has been achieved in establishing the mechanistic basis of the cold dwell fatigue phenomenon, the reasons why the alloys with differing Mo content show such stark dwell differences have not yet been elucidated. It is complicated because of the range of factors which may contribute (alloy composition, chemistry, crystallography, morphology, spatial and temporal scales, load shedding) which have recently been reviewed by Britton et al. (2015).

Cold dwell fatigue is normally associated with the formation of basal facets or microcracks (shown by Sinha et al. (2006) for Ti-6242), where the HCP alpha Ti crystal c-axes are oriented near-parallel to the primary loading direction (Bache, 2003; Evans and Bache, 1994). Variations of up to $\pm 15^\circ$ are anticipated since the basal stresses generated at a hard grain orientation (i.e. c-axis parallel to the loading) remain high and largely unchanged even with deviations of orientation up to 15° away from parallel. In addition, deviations also occur simply from the perturbations in the *local* maximum principal stress direction because of grain boundary constraint effects, relative to the remote applied loading. A particular crystallographic orientation combination, in which a (soft) grain well-oriented for slip sits adjacent to a badly oriented (hard) grain, is argued to be important for the nucleation of facets (Dunne et al., 2007a, 2007b) because of the high stresses developed at the hard-soft grain boundary. This work supported the Stroh (Stroh, 1954) hypothesis of a dislocation pile-up in a grain well orientated for slip terminating at a 'grain boundary' under remote applied loading leading to high stress in the adjacent grain. Stroh's model supports the necessary but not sufficient condition of crystallographic orientation combination to induce facet nucleation (Bache, 2003) but does not address the dwell effect and the role of time dependence (Dunne et al., 2007a). Hasija et al. (2003) was the first to introduce the concept of load shedding in titanium alloys and utilised crystal plasticity modelling to show that the slip occurring in the soft grain could lead to the redistribution of stress into the adjacent hard grain during the load hold. This results from the remarkably strong strain rate sensitivity in Ti alloys which occurs even at low (e.g. 20 °C) temperatures which has now been quantified at the single-crystal level (Jun et al., 2016c; Zhang et al., 2016a) and in alloys Ti-6242 and Ti-6246, at the macroscale (Qiu et al., 2014). Earlier research had already demonstrated that some titanium alloys experience strong creep and relaxation at low temperature (Neeraj et al., 2000; Suri et al., 1999). The temperature-dependent creep and load shedding behaviour of near-α alloy Ti–6Al was examined by Zhang et al. (Zhang et al., 2015) using crystal plasticity modelling to demonstrate that the dwell debit depends crucially on temperature and that the particular temperature leading to the worst case dwell debit is 120 °C in the alloy considered. The rate-sensitive behaviour of titanium alloys at room temperature is believed to be fundamentally related to the dwell fatigue debit during service because it leads to the establishment of load shedding and high basal stresses which are argued to be crucial for facet crack nucleation (Anahid et al., 2011; Dunne and Rugg, 2008; Kirane and Ghosh, 2008). Lefranc et al. (2008) and Gerland et al. (2009) observed facet nucleation in Ti-6242 under dwell fatigue loading at room temperature for which the crack nucleation was found to occur at the α-β interfaces in the two phase alloy that they considered. They found that the applied stress necessary to drive dwell fatigue was higher than the material's yield stress, likely because of the difficulty of finding the weakest crystallographic orientation combination in the conventional laboratory-sized specimens used. This remains a

potential problem with small test sample sizes since they are not necessarily representative of component-level behaviour because of volume effects (Britton et al., 2015). Pilchak (2014) and Pilchak and Williams (2010) have argued that hydrogen is important in facet growth and that it is potentially relevant in enhancing local planar slip, which may also be important in the facet nucleation process.

The Stroh model adopted by Bache (2003) for dwell fatigue considers a single slip line of dislocations which terminates leading to the development of a local stress concentration. Recent characterisation of single crystal slip using high resolution digital image correlation (Jiang et al., 2016) makes clear the very strong localisation of slip which occurs during deformation, which is challenging the resolution of modelling techniques such as crystal plasticity. However, the related but higher resolution technique of discrete dislocation plasticity (DDP) allows for explicit representation of dislocations and slip (Van der Giessen and Needleman, 1995). Recently, the rate-sensitive response originating from dislocation behaviour has been assessed and a new discrete dislocation model which allows for thermally-activated dislocation escape from obstacles has been developed (Zheng et al., 2016). As a result, the room temperature rate-dependent deformation of model Ti alloys which display strong creep and stress relaxation has been successfully captured, together with the corresponding grain-level dislocation and slip activity. Hence in this paper, in order to investigate the mechanistic basis of dwell fatigue recognising the crucial role of rate-sensitive material behaviour, and the strong localisation of slip, the rate-sensitive discrete dislocation methodology is utilised.

We first establish a rate-dependent crystal plasticity framework to reproduce the macroscopic response of Ti-624x (x=2 and 6) alloys under low-cycle fatigue (LCF) and low-cycle dwell fatigue (LCDF) loading (Qiu et al., 2014), particularly in order to extract the rate-controlling crystal-level material properties of these alloys; namely the activation energy associated with thermally activated dislocation escape. We then utilise the new rate-sensitive discrete dislocation model (Zheng et al., 2016), which adds low rate sensitivity arising from thermally-activated dislocation escape from obstacles to the conventional sources of high rate sensitivity of dislocation mobility and nucleation, which requires the activation energies obtained from the crystal plasticity model to examine the behaviour of Ti-6242 and Ti-6246 undergoing nano-indentation. In this way, assessment of the rate-sensitive discrete dislocation plasticity model with respect to independent experimental observations of rate-sensitive, single crystal indentation into Ti-6242 and Ti-6246 (Jun et al., 2016a) is achieved. We then employ the DDP model to investigate the grain-level slip and dislocation behaviour of the two alloys Ti-6242 and Ti-6246 under dwell fatigue conditions in order to address the long-standing technological question and its elusive solution: why is it that alloy Ti-6242 *does* show a dwell fatigue debit whereas Ti-6246 *does not*?

2. Modelling methodology

Both crystal and discrete dislocation plasticity modelling are utilised: the crystal-level model is employed to extract key crystal properties (e.g. slip strengths and activation energy for dislocation escape) from macro-level experimental observations. The discrete dislocation model, utilising the activation energies from the crystal-level modelling, is firstly tested against independent indentation experiments in the Ti-6242 and Ti-6246 alloys to assess in some detail the resulting rate sensitivity predicted by the DDP model and its comparison with that observed in the experiments. We then go on to utilise the DDP model to address dislocation behaviour at a hard-soft grain boundary interface in the context of the dwell fatigue phenomenon in these alloys. The details of the crystal plasticity and rate-sensitive discrete dislocation plasticity modelling methods respectively, have been described in full in earlier papers (Dunne et al., 2007a; Zhang et al., 2015; Zheng et al., 2016) and hence are covered only briefly in what follows.

2.1. Polycrystal modelling and the crystal plasticity slip rule

The rate-controlling slip process is based on the thermal activation of escape of pinned dislocations once an energy barrier is overcome in order to cause the release of pinned dislocations from obstacles, which glide once free. The plastic shear strain rate is determined from the average dislocation velocity given by Cottrell and Dexter (Cottrell and Dexter, 1954)

$$\dot{\gamma}^p = \rho_m v_g b \tag{1}$$

where b is the Burger's vector magnitude, ρ_m is the overall mobile dislocation density and v_g the average dislocation glide velocity. The average velocity is obtained by considering a mean obstacle spacing multiplied by the successful dislocation jump frequency. The frequency is derived in Dunne et al. (2007a), which is developed from a consideration of the Gibbs free energy (Gibbs, 1969), recognising both forward and backward dislocation activation events. When the resolved shear stress τ on a slip system exceeds a critical value τ_c, slip occurs and the shear strain rate is given by

$$\dot{\gamma}^p = \rho_m b^2 \nu_D \exp\left(-\frac{\Delta F}{kT}\right)\sinh\left(\frac{(\tau-\tau_c)\gamma_0 b^2}{kT\sqrt{\rho_o}}\right) \tag{2}$$

where ν_D is the frequency of attempts of dislocations to jump the energy barrier, ΔF the activation energy, k the Boltzmann constant, T the temperature, γ_0=6×10^{-4} a representative shear strain magnitude and ρ_o is the overall obstacle density which is taken to be 0. 01μm^{-2} giving an effective activation volume $\Delta V=\gamma_0 b^2/\sqrt{\rho_o}$. The slip system hardening in the model arises

from the increasing density of statistically stored dislocations ρ_{SSD} given by

$$\tau_c = \tau_{c0} + Gb\sqrt{\rho_{SSD}} \tag{3}$$

and for simplicity and in the absence of mechanistically informed methodologies for the evolution of statistically stored dislocations, the rate of evolution of the latter is simply taken to be directly related to the accumulated plastic strain rate, $\dot{p}$, by

$$\dot{\rho}_{SSD} = \gamma'\dot{p} \tag{4}$$

where τ_{c0} is the initial slip system strength, or critical resolved shear stress, G the shear modulus and γ' is the hardening rate.

Property values and geometric microstructure modelling to represent alloys Ti-6242 and Ti-6246 are described in a later section. However, the motivation for using crystal-level modelling needs to be established here in order to explain the simplifying assumptions made with respect to this modelling technique. The two alloys Ti-6242 and Ti-6246 are near-alpha but dual phase comprising the HCP alpha and BCC beta phases. The former alloy is bimodal and often globular in morphology comprising primary alpha grains and a distribution of grains of alpha-beta colony lath structures (Jun et al., 2016b). Even at a crystal modelling level, the alpha-beta grains are often homogenised to facilitate modelling (Anahid et al., 2011) and it transpires that the independent properties of the beta phase are not dramatically different to those of the alpha phase (Zhang et al., 2016b), such that this is not an unreasonable simplification. The latter alloy, Ti-6246, is in some ways rather more complex, being made up of a uniform distribution of single mode alpha-beta lath structures such that a homogenised representation is again generally reasonable. It is argued that it is the very much more anisotropic crystallography of the HCP alpha phase which drives the most important behaviours of these alloys. Indeed, the ⟨a⟩-type basal, prismatic, pyramidal, and ⟨c+a⟩-types I and II pyramidal slip systems have very different slip strengths, which have been quantified by Gong and Wilkinson (2011), and are shown schematically in Fig. 2.

The crystal modelling explicitly recognises the HCP alpha phase but does not do so for the beta laths such that the crystal properties extracted by reference to experimental data for these alloys are those of the homogenised alpha-beta behaviour.

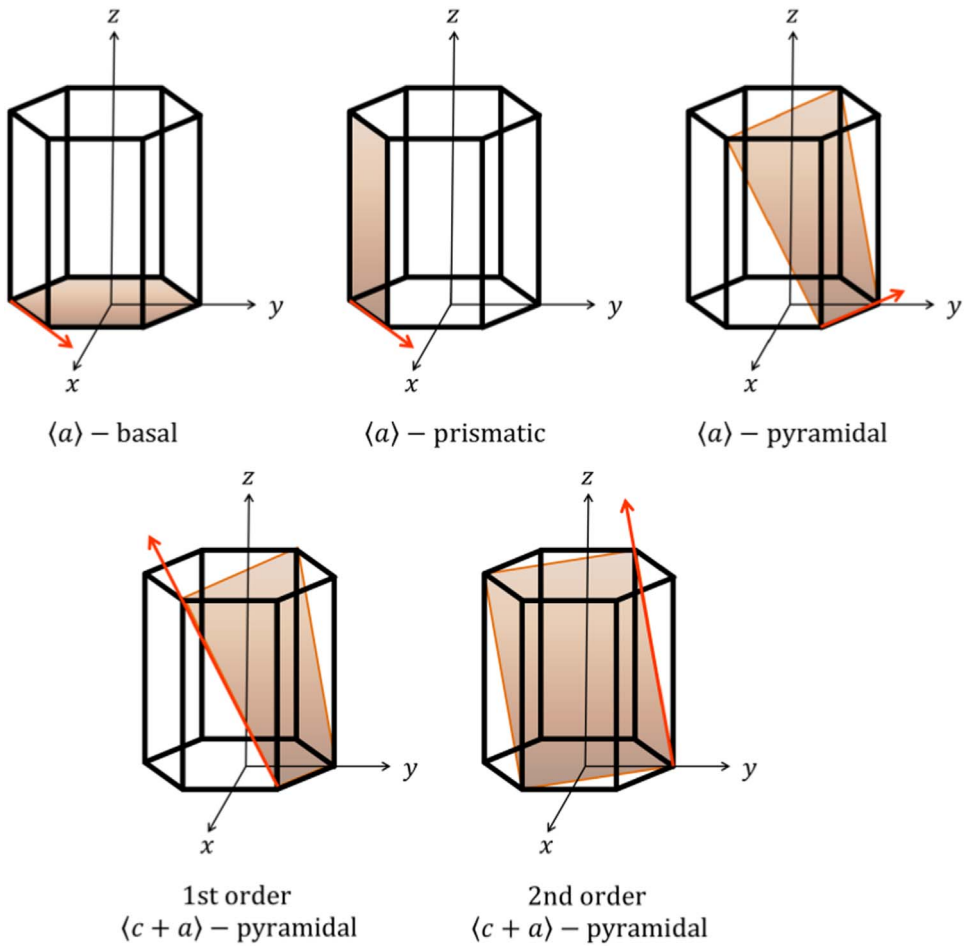

Fig. 2. Schematic diagrams showing ⟨a⟩-type basal, prismatic and pyramidal slip systems and ⟨c+a⟩-types I and II pyramidal systems.

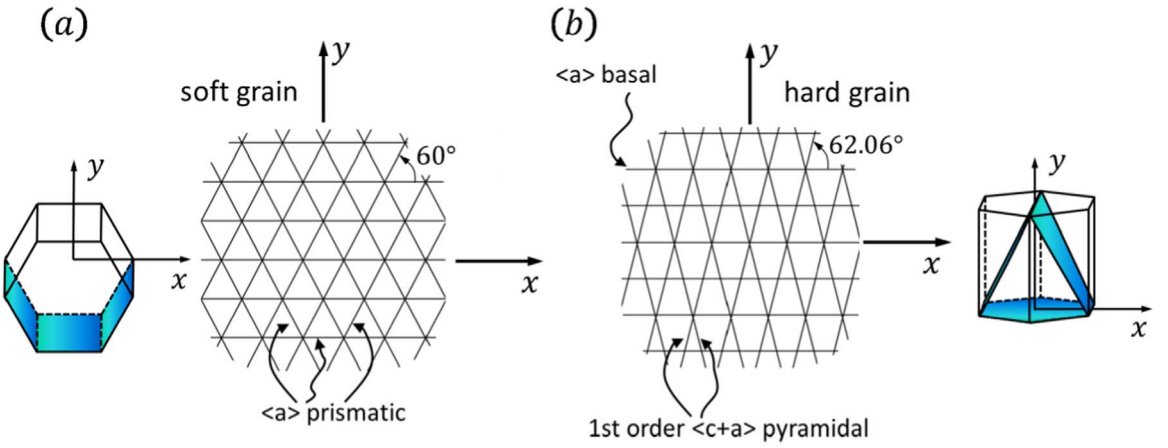

Fig. 3. Schematic diagrams of slip systems in the (a) soft grain and (b) hard grain which maintains the plane strain conditions.

However, this is argued to be justified in this context since the crystal plasticity modelling is carried out in order to extract the average, macroscale rate controlling activation energies for the two alloys, Ti-6242 and Ti-6246, which are to be employed in more detailed and representative discrete dislocation modelling. The Frank-Read source strengths for the two alloys in the DDP model are determined by calibrating with the polycrystalline rate-sensitive responses in the CP model. Further detail is provided in a later section, but in continuing to present the modelling methodology adopted, the rate-sensitive DDP model is described next.

2.2. Discrete dislocation plasticity formulation

A two-dimensional (plane strain) discrete dislocation plasticity formulation is employed to simulate polycrystalline behaviour, and this constrains, as a consequence, the combinations of slip that are allowed since they must be compatible with the plane strain constraint. Consider, for example, two adjacent grains, one well-aligned (soft) and the other badly aligned (hard) for slip. Of the HCP slip systems shown in Fig. 2, in order to maintain conditions of plane strain, only prismatic slip is allowed in the soft grain, and in the hard grain one basal slip system together with two 1st order $\langle c+a \rangle$ pyramidal slip systems are permitted. These combinations of orientations are depicted in Fig. 3(a) and (b) respectively. While the two-dimensional simplification reduces generality, it does not preclude physical insight into the mechanistic basis of the deformation processes taking place.

The generic boundary value problem is solved using the superposition method introduced by an der Giessen and Needleman (1995). Typically, 150 × 150 quadratic, rectangular finite elements are employed in the DDP model (to solve the boundary conditions correction problem) in order to obtain convergent results.

The polycrystals are taken to be stress and dislocation free at the beginning of the DDP calculation. Dislocation dipoles (cross-sections of loops taken through the pure-edge segments) are generated by Frank-Read sources that are randomly distributed on slip planes spaced $100b$ apart, with an overall density ρ_{nuc}. The source strengths are chosen to satisfy a Gaussian distribution with average $\bar{\tau}_{nuc}$ and standard deviation $0.2\bar{\tau}_{nuc}$. When the resolved shear stress at a source is greater than a nucleation strength τ_{nuc} for a period of time t_{nuc}, two edge dislocations with Burgers vector b and opposite signs are generated. The nucleation time is estimated by Agnihotri and Van der Giessen (2015) as

$$t_{nuc} = \eta \frac{\phi}{\tau b} \tag{5}$$

where 2ϕ is the source length and η is a constant related to the viscous drag coefficient B. The initial nucleation spacing L_{nuc} is taken such that the attraction stress between dislocations is equilibrated by the applied stress field τ_{nuc}.

After nucleation, dislocations glide on their slip plane with velocity v driven by the Peach-Koehler force τb governed by the mobility law

$$v = \frac{\tau b}{B} \tag{6}$$

When two dislocations of opposite sign move together within the annihilation distance $6b$, they are eliminated from the model. All grain boundaries are assumed to be impenetrable to dislocations. The gliding dislocations may also be obstructed by randomly distributed obstacles with a density of ρ_{obs}. Each obstacle is assigned a critical time t_{obs} which describes the required time for a pinned dislocation to escape by thermally activated escape, describing e.g. a climb or jog formation process. This is a key rate-controlling process relevant over strain rate ranges 10^{-5}–$10^{0}\ s^{-1}$, and the escape time is calculated from the inverse of the successful jump frequency, $t_{obs} = 1/\Gamma$; the latter has been developed by Zheng et al. (2016) to

be

$$\Gamma = \frac{\nu_D b}{l_{obs}} \exp\left(-\frac{\Delta F}{kT}\right) \sinh\left(\frac{\tau \Delta V}{kT}\right) \tag{7}$$

in which l_{obs} is the average obstacle spacing, and ΔV is the activation volume. The two key parameters controlling the rate sensitivity resulting from thermally activated dislocation escape are the activation energy ΔF and activation volume ΔV. From Eq. (7), it is seen that increasing activation energy leads to a higher energy barrier and as a consequence, a larger obstacle escape time. Conversely, increasing activation volume tends to diminish the thermal activation time.

The dwell fatigue response of the two alloys Ti-6242 and Ti-6246 is the main focus of this study, and it is necessary to establish their key mechanical properties. The methodology adopted is to utilise crystal plasticity modelling to represent the alloys' polycrystal, macro-level behaviour, and in so doing, characterise their respective slip system strengths, activation energies and activation volumes. These properties are then utilised within the rate-sensitive discrete dislocation model in order to provide lower length scale insight into dislocation behaviour at a hard-soft grain interface known classically to be important in cold dwell fatigue. This is addressed in the next section.

2.3. Determination of crystal plasticity and discrete dislocation model properties

The crystal plasticity model is addressed first in order to determine slip strengths, and activation energies and volumes for the Ti-624*x* alloys, and this is achieved using the recent experimental cyclic fatigue experiments of Qiu et al. (2014) who examined the low cycle fatigue and low cycle dwell fatigue of alloys Ti-6242 and Ti-6246. A simple polycrystalline model was established for this purpose and subjected to the low cycle and low cycle dwell fatigue loading in order to establish the average, macro-level response, but importantly, over many thousands of loading cycles to achieve the stabilised cyclic state, which necessitated long simulation times. The model consists of 16 square grains of 1 μm size which was subjected to the LCF and LCDF loading. The peak applied stresses imposed are 95% of the experimentally reported 0.2% proof stresses, i.e. 830 MPa and 954 MPa for Ti-6242 and Ti-6246 alloy respectively, as in the corresponding experiments (Qiu et al., 2014). The critical resolved shear stresses τ_c of both alloys were estimated by applying uniaxial displacement-controlled tension loading to give flow stresses as close as possible to the experimental results. Note that the prismatic and basal critical resolved shear stresses are taken to be the same, and the pyramidal (type I) CRSSs to be three times that of the prismatics. The activation energies ΔF were determined in order for the polycrystal model to replicate the plastic ratchet strain accumulations observed in the experimental LCDF observations. Finally, the hardening rates γ' were determined to capture the primary to secondary ratchet strain accumulation transition which occurs over the first 1000 LCDF cycles. The rate sensitivity of the crystal plasticity model is controlled by two properties (namely, activation energy and activation volume); this is identical to classical crystal plasticity and it is argued that a unique dependence is achieved over appropriate ranges of strain rate.

The resulting comparisons between average cyclic experimental measurement and the crystal plasticity calculations are shown in Fig. 4 for the Ti-6242 and Ti-6246 alloys for the loading cases of LCF and LCDF respectively (the nature of the loading is shown inset in the figures). It is noted that the accumulated plastic strains under LCF for Ti-6242 and Ti-6246 are similar giving rise to accumulated plastic strain magnitudes of less than 0.01 after 4000 cycles. Quite to the contrary however, under LCDF, the plastic strain for Ti-6242 is seen to accumulate rapidly with continuing, but stable ratcheting,

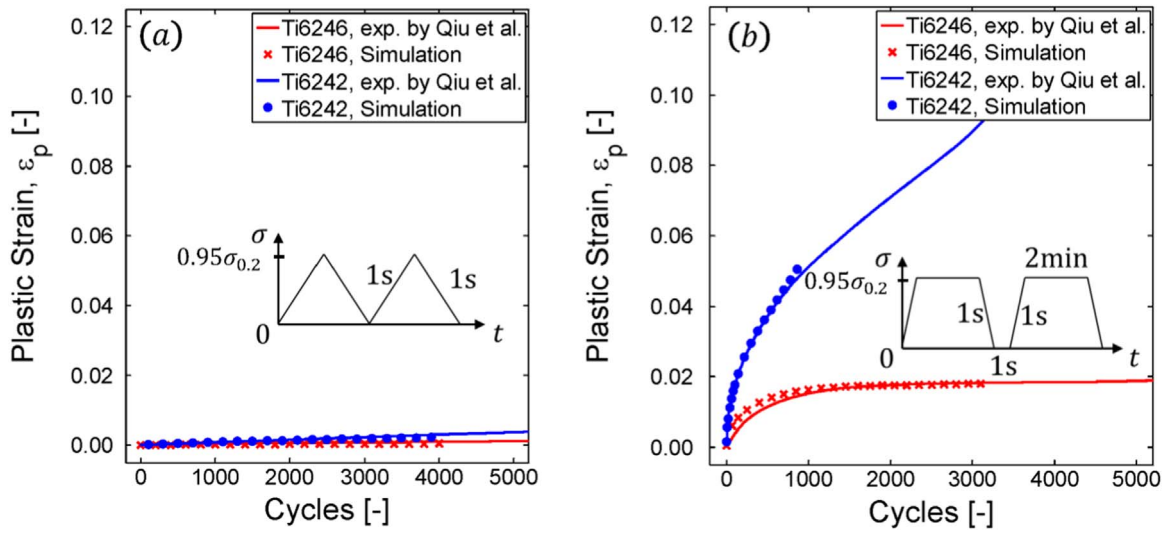

Fig. 4. Experimental and crystal model curves for Ti-624*x* under (a) LCF and (b) LCDF.

Table 1
Crystal plasticity slip rule properties.

	$\sigma_{0.2}$ (MPa)	τ_c (MPa)[a]	γ'	ΔF (J/atom)
Ti-6242	830	355	60	9.8×10^{-20}
Ti-6246	954	420	50	10.6×10^{-20}

[a] The critical resolved shear stress for the prismatic systems are given, but those for basal systems are taken to be the same as the prismatics, and those for (type I) pyramidal to be three times those of the prismatics.

while that for Ti-6246 reaches shakedown and a low peak magnitude of accumulated plastic strain (less than 0.02) after 1000 cycles. The polycrystal model is shown to provide good agreement with the experimental observations and the activation energies ΔF, prismatic slip strengths τ_c, and hardening rates γ' extracted for the two alloys in the crystal plasticity model are shown in Table 1, together with the equivalent 0.2% yield stresses $\sigma_{0.2}$. The critical resolved shear stress for the 1st order $\langle c+a\rangle$ pyramidal system is assumed to be three times that of prismatic slip, i.e. $3\tau_c$, based on the measurements of single crystal slip strengths from micro-cantilever bend tests on commercially pure Ti carried out by Gong and Wilkinson (2009). The experimental results of Qiu et al. (2014) shown in Fig. 1 make clear that the dwell debit for Ti-6242 is far greater than that for alloy Ti-6246, confirming that Ti-6242 is dwell sensitive whereas Ti-6246 is very much less so. The activation energy determined for Ti-6246 is found to be higher than that for Ti-6242 indicating that it is more difficult for pinned dislocations to escape from obstacles for the former alloy, giving rise to a higher average dislocation velocity for alloy Ti-6242.

In order to provide a further, independent assessment of the validity of the crystal plasticity properties extracted for the two alloys, additional comparisons with documented experimental measurement of their rate-sensitive responses is assessed. Strain-controlled uniaxial loading of the same simple polycrystal model as employed for cyclic loading but with three differing strain rates was imposed, utilising the crystal plasticity properties given in Table 1. The resulting calculated stress-strain responses of the two alloys under different strain rates are shown in Fig. 5(a). The predicted flow stress of Ti-6246 is found to be higher than that for Ti-6242 due to the higher critical resolved shear stress obtained, whereas the strain rate sensitivity manifested by these two alloys under uniaxial strain-controlled loading is predicted to be very similar. This is particularly interesting given the markedly different responses resulting from the inclusion of the dwell, both from experiment and model prediction in Fig. 4(b). We note that the crystal plasticity model gives predicted 0.2% proof stresses close to experimental measurements of Qiu et al. (2014), given in Table 1. In addition, Fig. 5(a) shows that the predicted flow stress differences arising from the order of magnitude differing strain rates imposed for the alloys are 31 MPa for both Ti-6246 and Ti-6242 respectively. The experimentally observed stress difference for Ti-6242 was observed by Neeraj et al. (2000) to be 33 MPa giving close agreement with the crystal model.

2.4. DDP model validation by comparing with nano-indentation tests of Ti-624x alloys

Experiments of nano-indentation into single crystal alpha grains contained within a polycrystal surface have been carried out by Jun et al. (2016a). Indentation into HCP basal and prism planes, selected from EBSD characterisation of the

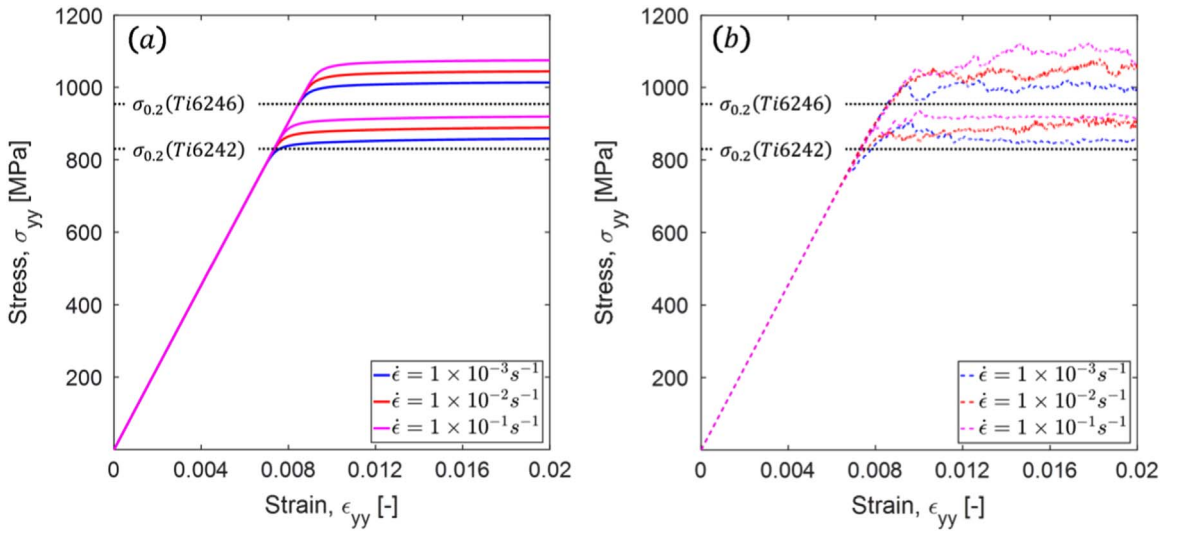

Fig. 5. Uniaxial tension for the strain rates shown for Ti-6242 and Ti-6246 using (a) crystal plasticity and (b) discrete dislocation plasticity modelling.

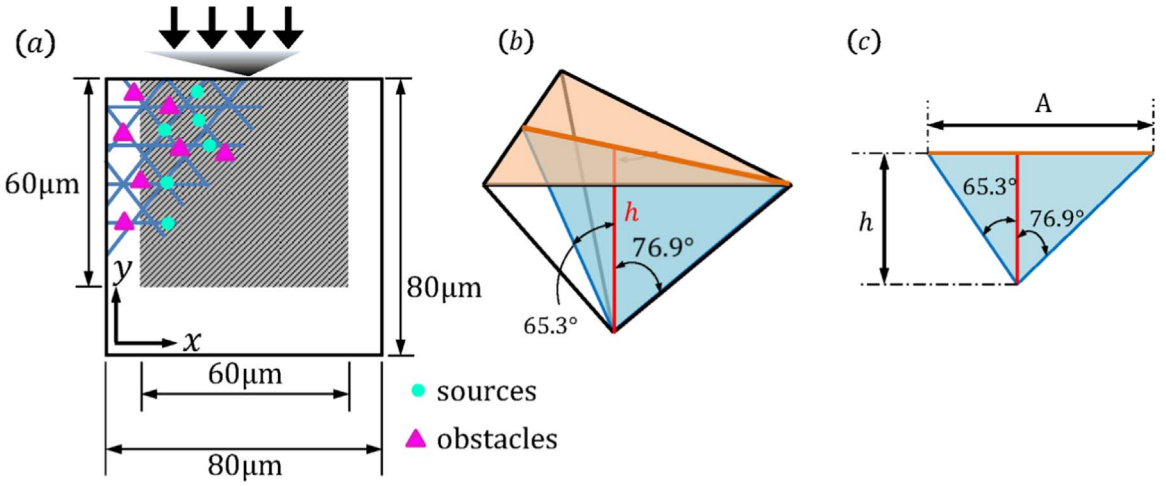

Fig. 6. (a) Schematic diagram of single crystal nano-indentation DDP model, in which Frank-Read sources are generated only within the shaded area while slip planes and obstacles are represented throughout; (b) perfect Berkovich indenter geometry and (c) the cross-section of the Berkovich tip, modelled in two dimensions.

surface, has been carried out for both Ti-6242 and Ti-6246 alloys in order to establish the single crystal strain rate sensitivities. Experiments were performed for four target indentation strain rates of 2×10^{-1}, 5×10^{-2}, 5×10^{-3} and 1×10^{-3} s^{-1} up to 2000 nm depth using a perfect Berkovich indenter. The nano-indentation 'strain rate' is defined as the indenter velocity divided by the indentation depth, i.e. $\dot{\varepsilon} = \dot{h}/h$ (Mayo and Nix, 1988), while the hardness H is defined as $H=P/A$, where P is the applied force and A is the projected area of the indent. The latter, for a perfect Berkovich tip, is given by $A=24.5h^2$. The material strain rate sensitivity is then given by

$$m = \frac{\mathrm{d}(\ln H)}{\mathrm{d}(\ln \dot{\varepsilon})} \tag{8}$$

Full details of the experiments may be found in Jun et al. (2016a).

Fig. 6(a) shows a two-dimensional schematic of the indentation set-up in order to develop a representative DDP model. In two dimensions, only the cross-section of the indenter is modelled and the resulting geometry of the cross-section is illustrated in Fig. 6(b) and (c), from which the projected area can be calculated as $A=6.47h$. The model sample dimensions are 80 μm × 80 μm but the nucleation sources are only distributed in the greyscale shaded area shown around the indenter to avoid dislocation nucleation in the model sample bottom corners. This is appropriate since in the experiments, the sample surfaces are far removed from the indenter region, and these conditions are approximately reproduced in the sample model as described. The slip planes and obstacles are distributed over the complete model crystal sample. The sample free boundaries are all subjected to displacement boundary conditions of $u_x = u_y = 0$. The resulting predicted material pile-up together with the yy-stress distribution after indentation for a source-free model are shown in Fig. 7(a) and (b) respectively, from which a stress concentration around the indentation site can be observed. The finite element mesh was refined around the indenter tip, as shown Fig. 7(a), with a minimum mesh size of 0. 005 μm and consisting of 120 × 80 bilinear elements as detailed in Balint et al. (2006). The DDP model calculations were performed on grains giving basal and prism plane indentation, for both alloys Ti-6242 and Ti-6246, as in the experiments.

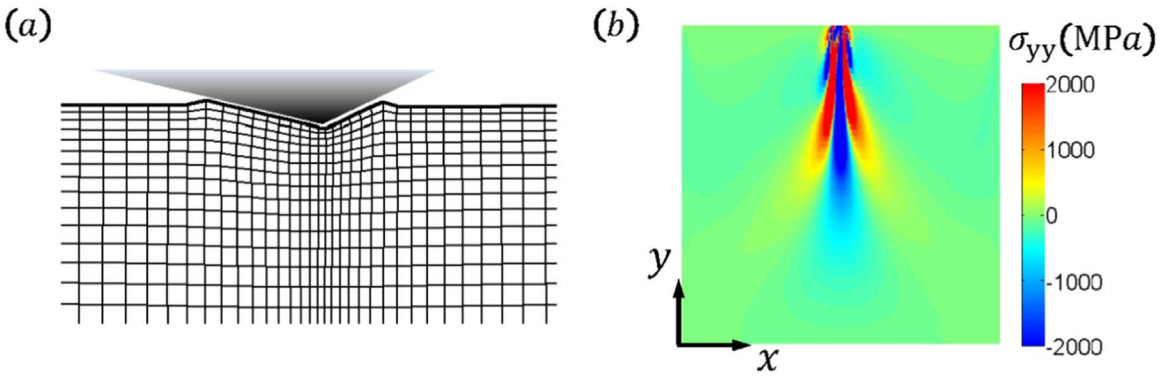

Fig. 7. (a) Deformed mesh around the indenter (b) yy-stress distribution after indentation for a source-free model.

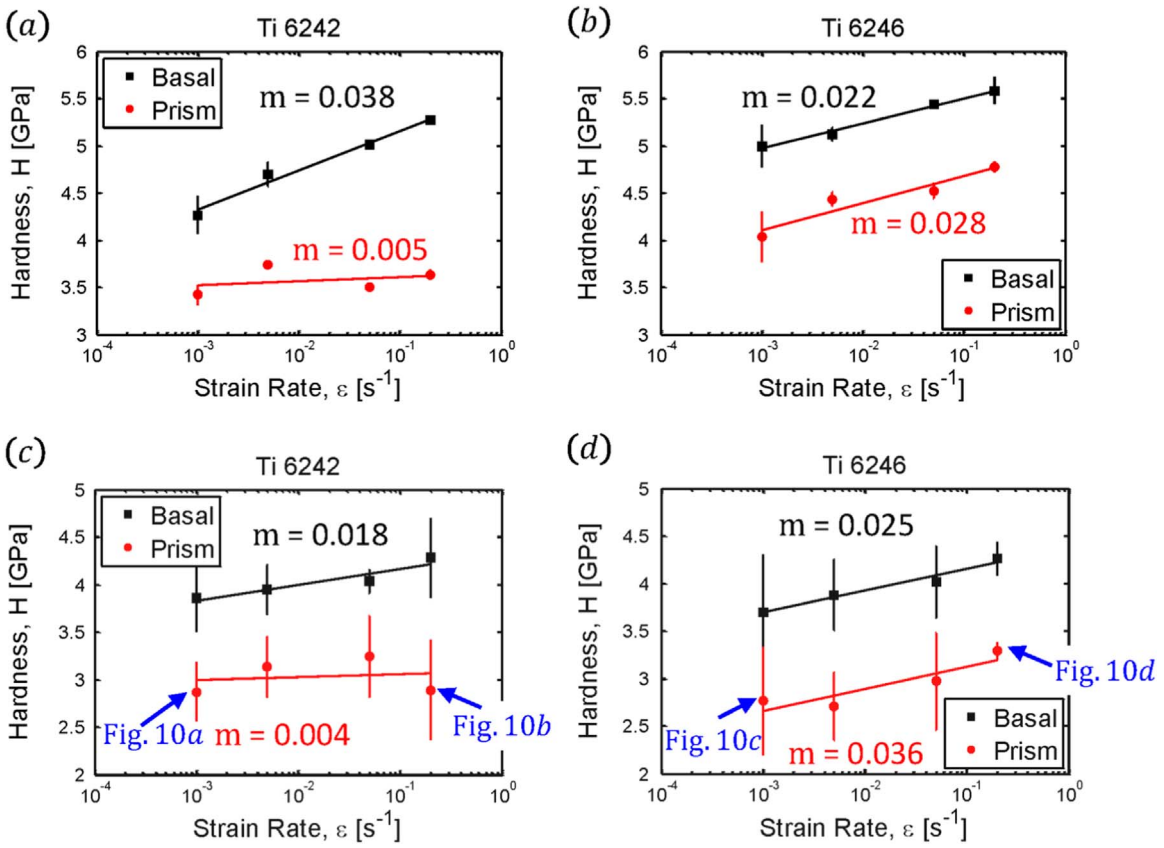

Fig. 8. Hardness vs. strain rate (log-log form) obtained from experimental observation of (a) Ti-6242 and (b) Ti-6246, and the DDP predicted results for (c) Ti-6242 and (d) Ti-6246 for nanoindentation Four sets of model nanoindentation conditions are identified to compare the dislocation density and stress states in later figures.

The experimental measurements and DDP predictions of the strain rate sensitivities for the two alloys and two indentation directions relative to the crystal structure are shown in Fig. 8. For each strain rate test (in both experiment and simulation), an average of four tests was used to evaluate the rate sensitivity m with the standard deviations displayed as an error bar in the graphs. The experimental results in Fig. 8(a) and (b) for Ti-6242 and Ti-6246 respectively reveal a higher rate sensitivity for the indentation into the basal plane (i.e. crystal orientation as shown in Fig. 3(b)) when compared with indentation into the prism plane (Fig. 3(a)) in Ti-6242. On the other hand, the basal and prism plane indentations show comparable rate sensitivities in Ti-6246. In other words, the indentation experiments suggest Ti-6242 experiences a strong crystallographic-orientation-dependent rate sensitivity while Ti-6246 does not. Fig. 8(c) and (d) from the DDP model predictions show that similar overall results are obtained in that the differences in rate sensitivities for the differing plane indentations are small for alloy Ti-6246 but much larger for alloy Ti-6242. The magnitudes of the rate sensitivities show qualitative agreement only and the quantitative difference likely arises because of the two-dimensional nature of the DDP model.

In order to understand why the indentation into the prism plane of Ti-6242 alloy shows such low rate sensitivity, a parametric study has been carried out to investigate the effect of activation energy on the local rate sensitivity of nanoindentation tests. Three representative activation energies, 9.8×10^{-20} J/atom (same as Ti-6242), 10.6×10^{-20} J/atom (same as Ti-6246) and 12.0×10^{-20} J/atom, are selected and the rest of the material constants are the same as the Ti-6242 prism indentation model specimen. As shown in Fig. 9, the rate sensitivity as well as the overall hardness increased with increasing activation energy. The high energy barrier makes the material difficult to deform, hence the hardness increased. The thermally activated dislocation escape events control the local rate sensitivity (Zheng et al., 2016), and under such highly concentrated loading conditions, the large time constant associated with dislocation escape leads to the sensitivity of the loading rates considered.

Information from beneath the experimental sample surfaces is not available from the experiments, but the DDP may be used to access this. The overall dislocation densities after indentation of the prism plane for both alloys under two selected strain rates are compared in Fig. 10. A high density of dislocations is seen to concentrate around the indenter tip. At low strain rate, the predominant rate-controlling mechanism is that of thermally activated dislocation escape (Zheng et al., 2016). In the area close to the indenter, the stresses are high (decreasing approximately inversely proportional to the distance from the indenter) so that all dislocations overcome the energy barrier and continue to glide. In other words, the motion of dislocations in this region is unlikely to contribute to the rate sensitivity of the crystal indentation. The

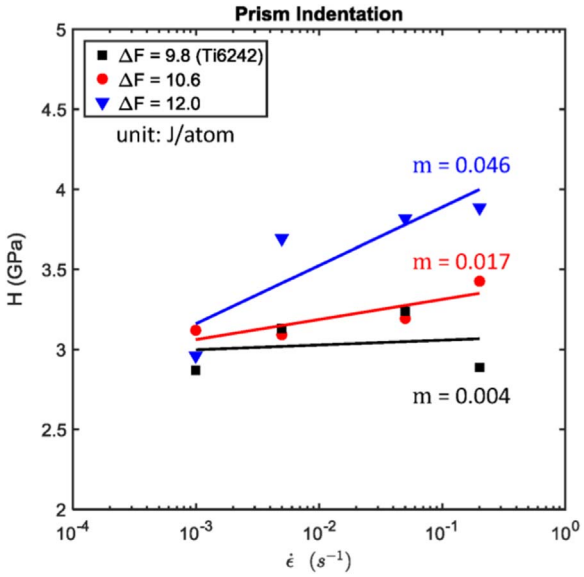

Fig. 9. Effect of activation energy on rate sensitivity of Ti-6242 prism system indentation. The activation energies have units of 1×10^{-20} J/atom.

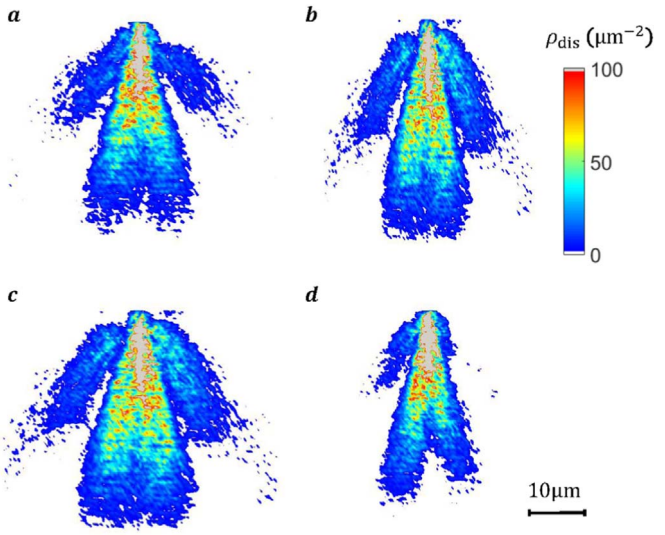

Fig. 10. Dislocation density contours after prism indentation at strain rates of 1×10^{-3} s^{-1} and 2×10^{-1} s^{-1} respectively for (a) and (b) Ti-6242 alloy, and (c) and (d) Ti-6246 alloy (as indicated in Fig. 8).

dislocations further away from the indenter are likely those giving rise to the rate-sensitivity. These dislocations originate from both direct nucleation from the Frank-Read sources away from the indenter and the longer distance gliding dislocations from the indentation area. Fig. 10(a) and (b) for Ti-6242 show rather similar distributions of dislocation densities at both low and high indentation rates. However, for alloy Ti-6246 in Fig. 10(c) and (d), the dislocation densities are quite different for the different rates. This is due to the low energy barrier in Ti-6242, such that dislocation escape from obstacles is enhanced, which results in the similar distributions of dislocations over the entire indentation rate range. However, for Ti-6246, the high activation energy leads to a longer dislocation escape time, comparable to the loading time. At high strain rate, the dislocations pile up at obstacles even in the high stress region near the indenter because they do not have sufficient time to escape, hence the dislocation density spatial reach is smaller than that for the low strain rate. The interesting consequence is that over the range of indentation rates considered, the low activation alloy Ti-6242 shows limited rate sensitivity since dislocation escape is so easy. The high activation energy alloy, Ti-6246, however, does show rate sensitivity since at the low indentation rate, escape is facilitated but it is inhibited at the higher rate.

This is not obviously intuitive from the macro-level response of the two alloys shown in Fig. 4 in which at the loading rates considered, it is the Ti-6242 alloy that shows the strongest rate sensitivity. The key difference, of course, is the rate regime at which the loading is occurring. In other words, the thermal activation of dislocation escape has associated with it a

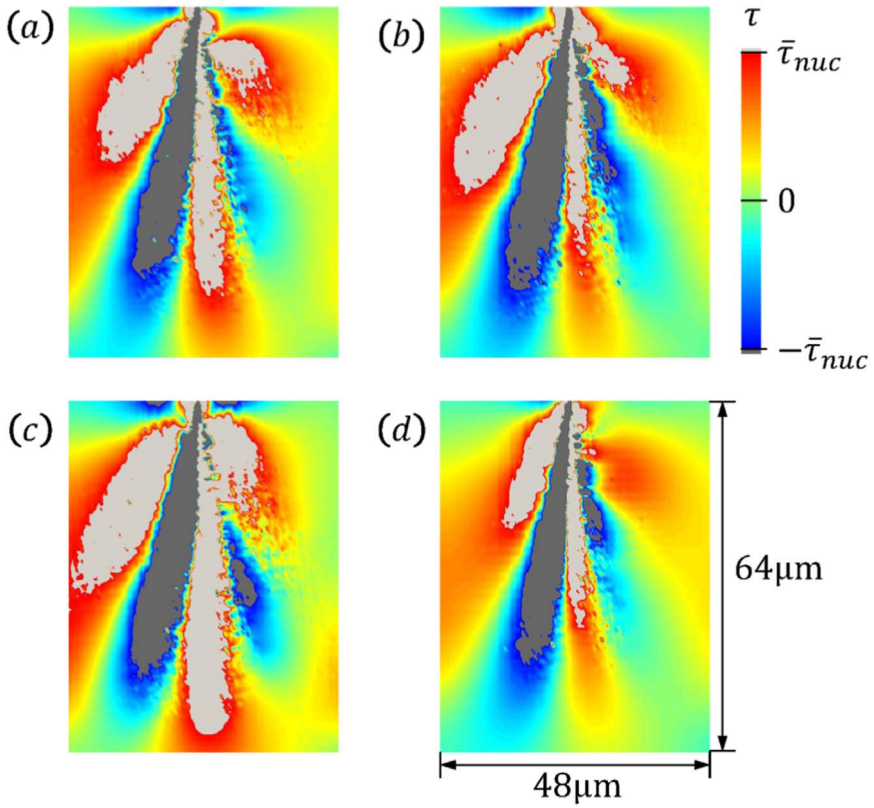

Fig. 11. The resolved sheared stress on the tilted ⟨a⟩-prismatic slip system in the soft grain of Ti-6242 under strain rate of (a) $1 \times 10^{-3}\,s^{-1}$; (b) $2 \times 10^{-1}\,s^{-1}$ and Ti-6246 under strain rate of (c) $1 \times 10^{-3}\,s^{-1}$; (d) $2 \times 10^{-1}\,s^{-1}$.

time constant (see Zheng et al., 2016 for details). If the time frame associated with the loading is of the order of the thermal activation time constant, a rate sensitive response is to be observed, but any significant difference (be it positive or negative) leads to the diminution of the apparent rate sensitivity. However, the thermal activation energy ΔF remains an intrinsic crystal property and determines its rate-sensitive response.

When we compare the resolved shear stress on the ⟨a⟩-prismatic slip systems oriented 60° with respect to the positive x-axis for prism plane indentation for both alloys as shown in Fig. 11, the differences for the two strain rates resulting for Ti-6246 are very visible (in (c) and (d)), but very little difference has developed for Ti-6242 (in (a) and (b)). In the case of high rate indentation in Ti-6246, obstacles pin dislocations, but with a high activation energy escape is inhibited resulting in the localisation of high shear. A consequence is that in Ti-6246, with higher activation energy, a rate sensitivity becomes apparent over the range of indentation rates studied. In the lower activation alloy Ti-6242, dislocation escape is so rapid that over the indentation rate range considered, little rate sensitivity is apparent.

3. Load shedding in Ti-624*x* alloys: the origin of dwell debit

The manifestations and some consequences of the differing activation energies for thermally activated dislocation escape associated with alloys Ti-6242 and Ti-6246 have been addressed. We focus in this section on consequences in terms of the *load shedding* at hard-soft grain combinations in oligocrystals which has been argued to be a key factor in controlling the dwell fatigue debit in these alloys (Dunne and Rugg, 2008; Dunne et al., 2007a; Hasija et al., 2003; Zhang et al., 2015). The rate-sensitive discrete dislocation formulation is employed to analyse polycrystalline behaviour, and a schematic diagram of the polycrystal representation is shown in Fig. 12(a), which is subject to stress-controlled loading that includes a stress hold in order to induce dwell fatigue effects. A controlled Poisson Voronoi tessellation has been used to generate the crystal morphology using the VGRAIN software system (Zhu et al., 2014). An average 15 μm^2, minimum 10 μm^2, and maximum 20 μm^2 grain size have been specified with a regularity parameter of 0. 9. A rogue grain combination is located in the central region of the model for which the crystallographic orientations are shown in Fig. 12(b). The polycrystal orientation distribution in the model is indicated in Fig. 12(c), from which one hard grain (red symbols) with c-axis orientated parallel to the remote loading and the remaining soft grains (black symbols) may be seen. The loading and boundary conditions imposed are illustrated in Fig. 12(a): a uniaxial stress-controlled tension is applied on the top surface while the bottom and

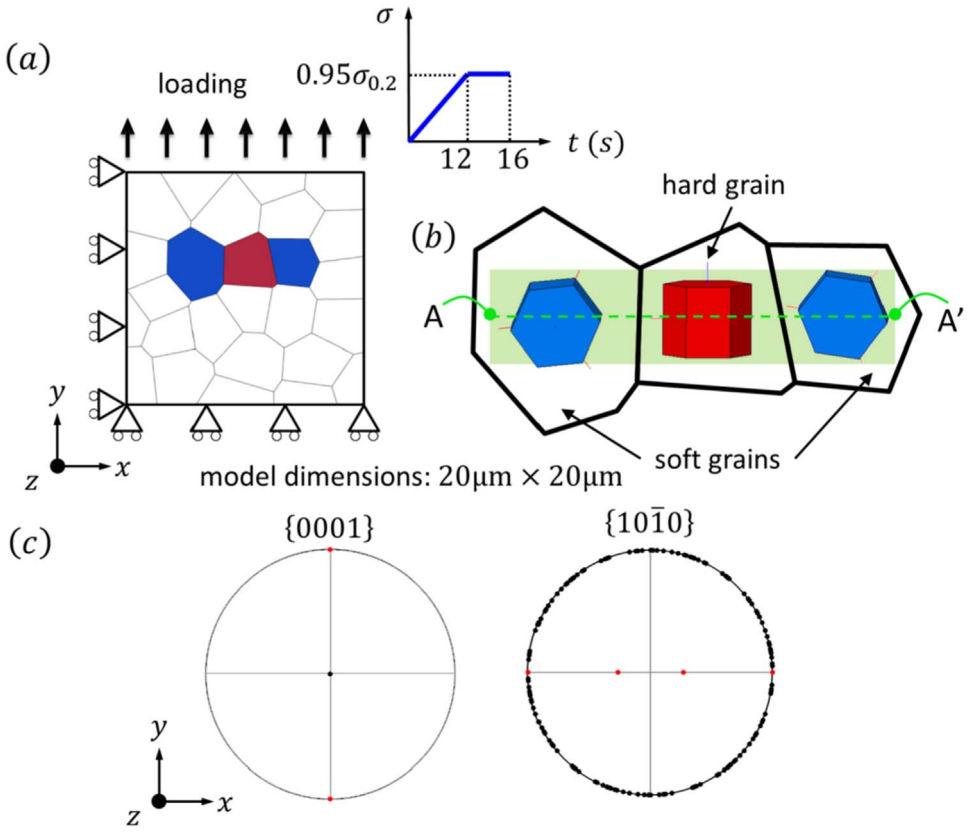

Fig. 12. (a) The DDP model geometry together with the crystal morphology; (b) local crystallographic orientations of the rogue grain combination; (c) pole figures of the polycrystalline DDP model, in which red symbols represents the hard grain while the black symbols represent all other (soft) grains. (For interpretation of the references to color in this figure legend, the reader is referred to the web version of this article.)

left surfaces are constrained as indicated. The imposed stress is increased at a constant rate until it reaches 0.95 of the yield stress $\sigma_{0.2}$ in 12 s, after which a stress hold at maximum magnitude 0. $95\sigma_{0.2}$ is imposed for 4 s. The yield stresses $\sigma_{0.2}$ are determined from the polycrystalline rate sensitivity study (as shown in Fig. 5) as 850 MPa and 1010 MPa for Ti-6242 and Ti-6246 at $\dot{\varepsilon}$=1×10^{-3} s^{-1}, respectively. The loading is purposefully chosen to give remote stresses that are lower than the macro-scale yield since this is deemed most relevant for in-service conditions. Also, it proactively negates the potential problem sometimes observed experimentally where much higher applied stresses are chosen in order to cause facet nucleation, but which may not therefore be relevant to the cold dwell fatigue mechanism.

The polycrystal in Fig. 12(a) is subjected to uniaxial loading along the y direction and the yy-stress distribution along the $A - A'$ path as shown in Fig. 12(b) is recorded during the loading history, and in particular, at the beginning of the load hold (or dwell) and at the end, as shown in the inset figure in Fig. 12(a). The stress along the path is strongly affected by the position of $A - A'$, e.g. if the path passes through a group of piled-up dislocations, the stress at that point becomes much higher than the average stress within that region. Hence, to begin, an average of the yy-stress along 20 paths which are all parallel to $A - A$' and are within the hard-soft grain boundary, i.e. within the shaded area shown in Fig. 12(b), is assessed to examine the stress through the rogue grain combination.

The Frank-Read source strengths are chosen as 480 MPa and 560 MPa for Ti-6242 and Ti-6246 respectively so that the DDP model shows similar stress response as the CP model under displacement control, as shown in Fig. 5, and all other properties for the two alloys are as detailed in Table 2. The resulting average yy-stresses along path $A - A'$ before and after the stress dwell are shown in Fig. 13 for Ti-6242 and Ti-6246 in (a) and (b) respectively. The differences in the observed load shedding are remarkable. The alloy Ti-6242 shows very significant redistribution of stress to the hard grain during the stress dwell, increasing at the soft-hard boundary from 1300 MPa to just over 2000 MPa. The orientation of the hard grain is such that the yy-stress is, in fact, the normal stress to the crystal basal plane so that the load shedding has led to an average tensile basal stress of 2000 MPa in the Ti-6242 alloy. However, the response is completely different for the Ti-6246 alloy where effectively, load shedding is simply not observed and the peak basal stress remains at about 1100 MPa. The difference between the two alloys could not be more stark and at first observation, provides compelling evidence that it is the differing rate sensitivities which drive the experimentally observed dwell debit difference.

Although the Frank-Read source strengths are chosen to give model flow stresses to be close to experimental observation, the source strength also apparently has a significant effect on the load shedding mechanism. A parametric

Table 2
Model parameters used in polycrystalline DDP model.

G (MPa)	ν	ρ_{nuc} (μm^{-2})	T (K)	η
29022	0.46	10	293	$90B$
ν_D (Hz)	k ($J K^{-1}$)	ρ_{obs} (μm^{-2})	b (nm)	B (Pa s)
10^{11}	1.38×10^{-23}	200	0. 32	10^{-4}
$\bar{\tau}_{nuc}$ (MPa)		ΔF (J/atom)		ΔV
Ti-6242	Ti-6246	Ti-6242	Ti-6246	Ti-624x
480	560	9.8×10^{-20}	10.6×10^{-20}	0. $5b^3$

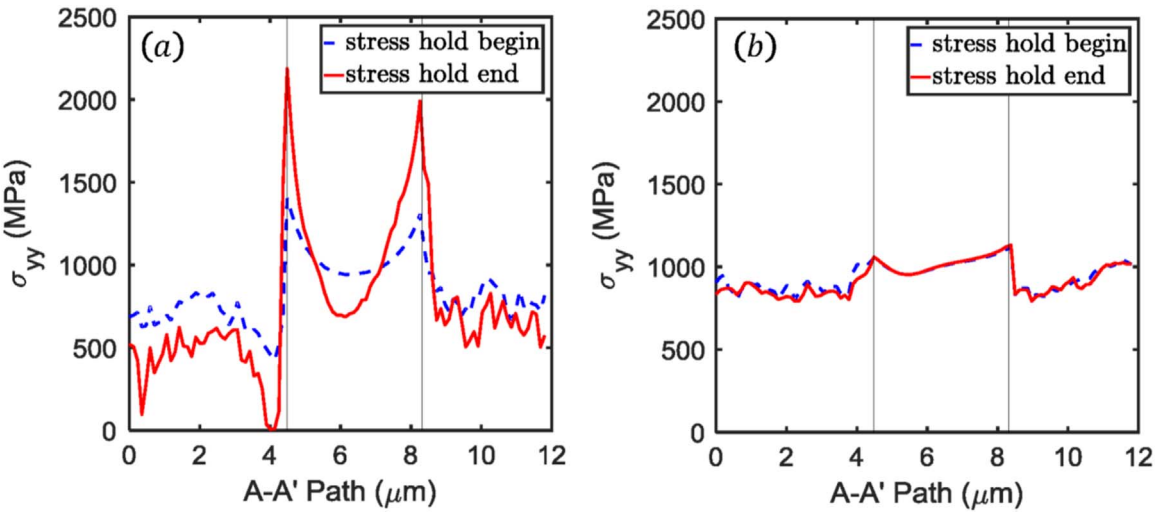

Fig. 13. The *yy*-stress along the A–A' path for (a) Ti-6242 and (b) Ti-6246 before and after the dwell.

analysis was carried out in order to understand the influence of source strengths. Two model alloys were compared with the Ti-6242 and Ti-6246 alloys: model alloy A: $\bar{\tau}_{nuc}$=480 MPa, $\Delta F = 10.6\times10^{-20}$ J/atom and model alloy B: $\bar{\tau}_{nuc}$=560 MPa, $\Delta F = 9.8\times10^{-20}$ J/atom with all remaining properties the same as shown in Table 2. The resulting average yy-stresses along path A – A' before and after the stress dwell are shown in Fig. 14. By comparing Ti-6242 (Fig. 13a) and model alloy A (Fig. 14a), which has the same low source strength, it is observed that both of the alloys show strong load shedding during the stress dwell period but the peak stress increase is lower when the activation energy is higher. On the other hand, when the alloys have high source strength, model alloy B (Fig. 14b) with low energy barrier starts to show load shedding compared

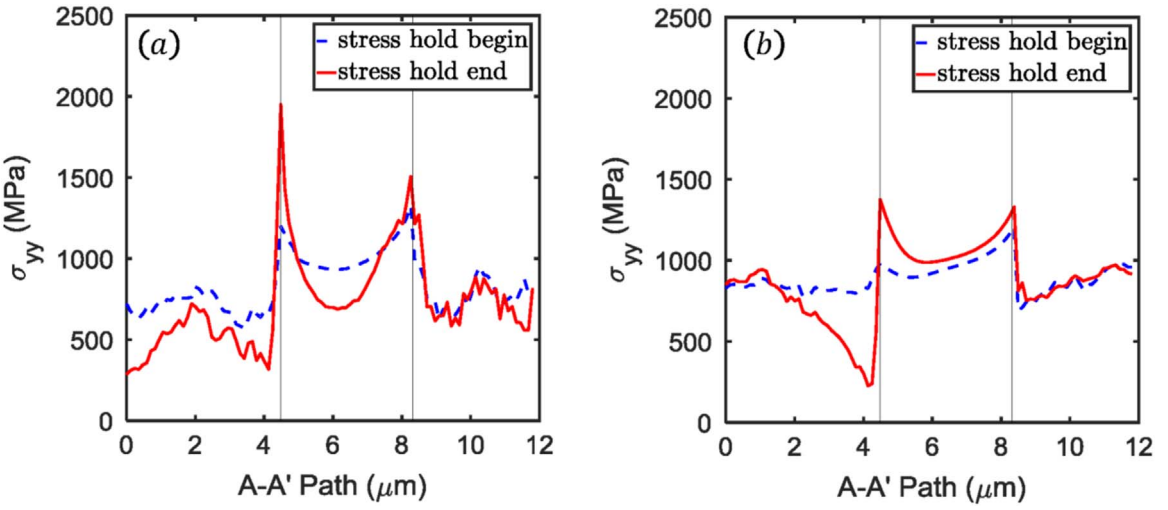

Fig. 14. The *yy*-stress along the A–A' path for (a) model alloy A with $\bar{\tau}_{nuc}$=480 MPa, $\Delta F = 10.6\times10^{-20}$ J/atom and (b) model alloy B with $\bar{\tau}_{nuc}$=560 MPa, $\Delta F = 9.8\times10^{-20}$ J/atom before and after the dwell.

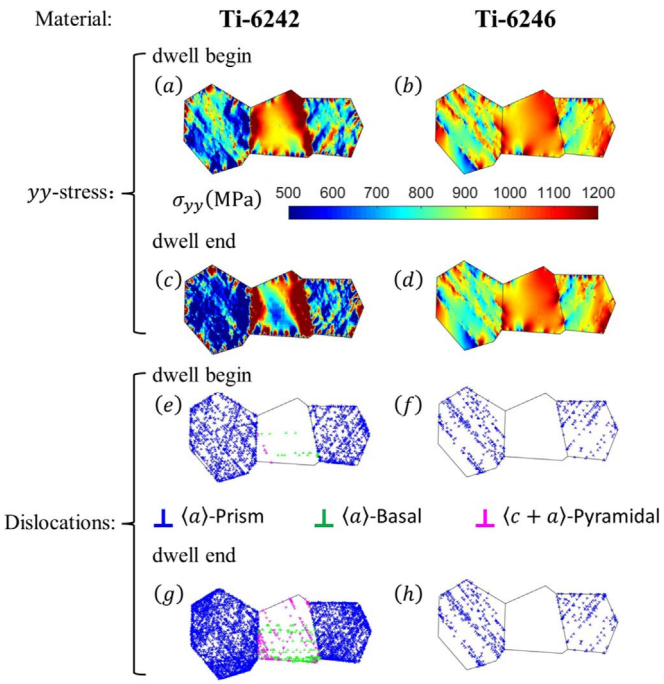

Fig. 15. The *yy*-stress contours and corresponding dislocation structures in the rogue grain combination before and after the dwell, shown for Ti-6242: (a)/(e) dwell begin, (c)/(g) dwell end; and for Ti-6246: (b)/(f) dwell begin; (d)/(h) dwell end.

to Ti-6246 (Fig. 13b), but the peak stress increased of approximately 400 MPa which remains considerably lower than for Ti-6242 alloy (about 700 MPa). From the above analysis, three categories with different behaviour can be identified: (i) both the Frank-Read source strength and the activation energy are low, giving strong load shedding during the dwell period; (ii) both the Frank-Read source strength and the activation energy are high, giving load shedding which is negligible; (iii) the Frank-Read source strength is low and the activation energy is high, or the Frank-Read source strength is high and the activation energy is low, giving partial load shedding.

Recall from Fig. 1 that alloy Ti-6242 shows very high dwell fatigue debit whereas Ti-6246 does not suffer a significant dwell debit at all. The mechanistic explanation for this difference has remained elusive. In light of the discussion earlier, the significant differences apparent in Fig. 13 result from the proximity of the time constant for thermally activated dislocation escape for the two alloys with that of the loading time scale. For the latter, the stress dwell chosen in this work is 4 s for reasons of computational time. However, it is well acknowledged and demonstrated that at temperatures in the vicinity of 20 °C, the critical dwell durations over which the stress relaxation is seen to occur is on the order of 60 s (Bache et al., 1997; Ozturk et al., 2016; Zhang et al., 2015). But in fact, most of the relaxation takes place over the first 12 s so that the dwell period used in this study is entirely indicative. So far, average stresses at the soft-hard grain boundary have been assessed, but potentially, strong localisations occur and this is addressed next.

Fig. 15 shows the spatial distribution of yy-stress and dislocation distributions (by type) at the beginning and end of the stress dwell for the two alloys. A first observation is that there is significantly more dislocation generation and pinning occurring for alloy Ti-6242 compared to that for Ti-6246. The differences are very marked. In addition, reflecting the earlier discussion, the stresses seen for Ti-6242 tend to be low in the soft grain and very high in the hard grain, and become higher and more localised at the hard grain boundary regions after the dwell period. For alloy Ti-6246, however, the spatial distribution of stress shows that the low stress magnitude is retained despite the stress dwell and remains rather homogeneous within the grain combination for Ti-6246. Hence the spatial distributions of stress and dislocation densities support the load shedding differences presented in Fig. 13.

Since the dislocation source strength is lower in the Ti-6242 alloy, the dislocations are easier to nucleate and due to the lower activation energy, the pinned dislocations find it easier to overcome the obstacle energy barrier and escape. Once pinned dislocations escape from obstacles, the long range back stresses acting on sources reduce. Sources are then able to reactivate and add further dislocations to the pile-ups at grain boundaries, which exacerbates the stress concentrations there. The dislocation pile-up groups develop the stress concentrations at the boundaries. Although the remote applied stress is perpendicular to the basal slip systems in the hard grain, i.e. the resolved shear stress on the basal plane (at least due to the global stress) is zero, the local stress state is different from the global stress because of the local spatial variation in elastic anisotropy and grain boundary constraint. A consequence is that Frank-Read sources located close to the grain boundaries nucleate. During the stress dwell, the sources in the soft grains keep activating and more dislocations reach the grain boundaries. As a result the stress concentration local to the grain boundaries increases and activates more basal

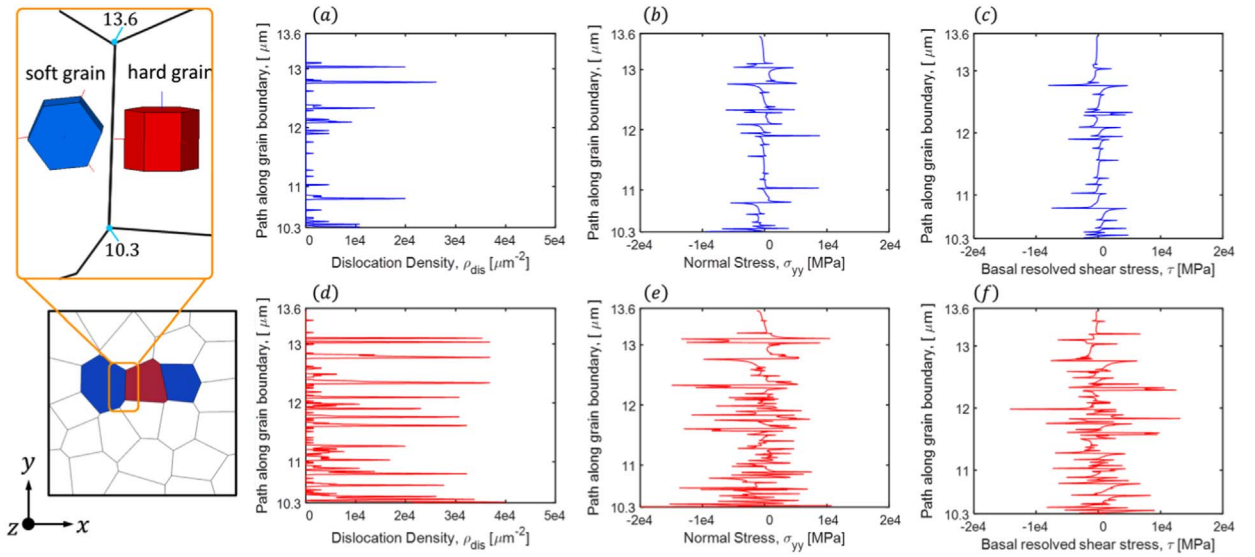

Fig. 16. Analysis along the soft-hard grain boundary in Ti-6242 before (a)–(c) and after (d)–(f) stress dwell. (a)/(d) dislocation density, (b)/(e) *yy*-stress and (c)/(f) resolved shear stress on the basal slip system in the hard grain.

sources together with $\langle c + a \rangle$ pyramidal sources. The redistribution of the stresses in the soft grain to the adjacent hard grain occurs by the generation of more dislocations which gives rise to the load shedding phenomenon observed in Fig. 13(a).

On the contrary, for alloy Ti-6246 as shown in Fig. 15, the stress levels in the soft and hard grains remain largely unchanged during the stress dwell period. The source strength is higher in Ti-6246 which tends to inhibit dislocation activation, hence there are less dislocations generated. On the other hand, the obstacle escape energy barrier is higher in Ti-6246 which inhibits pinned dislocations escaping from obstacles. In the absence of pinned dislocation escape, the back stresses are not relieved so that dislocation sources remain inactive. It can be seen that most of the dislocations generated in Ti-6246 remain distributed within the bulk of the soft grains as opposed to piling up at grain boundary as in alloy Ti-6242. In the absence of the stress concentration at the grain boundaries, there is no basal nor $\langle c + a \rangle$ pyramidal dislocation activity in the hard grain. In the Ti-6242 alloy, however, both dislocation types, perhaps unexpectedly including the $\langle c + a \rangle$ pyramidals, are activated in the hard grain as shown in Fig. 15.

The dislocation density distributions together with stresses along the soft-hard grain boundary within the hard grain are detailed and compared in Fig. 16 (Ti-6242) and Fig. 17 (Ti-6246). It can be seen that for Ti-6242 in Fig. 16, the dislocation density increases significantly after the dwell period consistent with earlier analysis. The significant dislocation pile up at

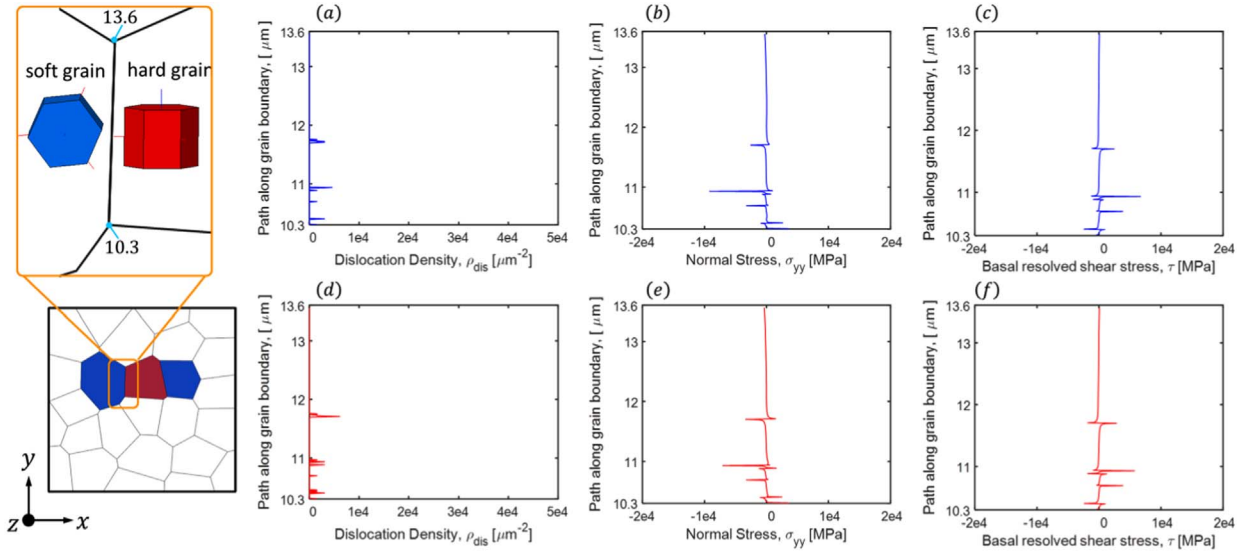

Fig. 17. Analysis along the soft-hard grain boundary in Ti-6246 before (a)–(c) and after (d)_(f) stress dwell. (a)/(d) dislocation density, (b)/(e) *yy*-stress and (c)/(f) resolved shear stress on the basal slip system in the hard grain.

the grain boundary leads to the development of high normal stresses to the basal plane in the hard grain which is potentially associated with facet crack nucleation and high basal resolved shear stress which gives rise to the basal slip nucleation in the hard grain. Corresponding results for alloy Ti-6246 in Fig. 17 show that only a few activated slip planes intersect the grain boundary since in the case of these particular planes, there are no obstacles located between nucleation sources and the grain boundary, which occurs because of the stochastic nature of the DDP analysis. Dislocations on these particular slip planes are free to glide to the boundary once generated. Other dislocations are observed to be nucleated on these planes during the stress dwell. Both the normal stresses and resolved shear stresses associated with the basal slip plane in the hard grain are negligible in Ti-6246 in comparison to alloy Ti-6242.

The uniaxial stress-strain response of the two alloys under displacement-controlled loading (Fig. 5) was found to be similar, but remarkably different under conditions of stress-controlled dwell loading (Fig. 4(b)). In the displacement-controlled loading, the same strain (0. 02) was applied to the two alloys, which requires the generation of similar numbers of dislocations to accommodate the total strain. Since Ti-6242 has lower source strength and lower activation energy, the dislocations are easier to generate, and then easier to escape from obstacles, giving rise to a higher overall glide velocity than for Ti-6246. However, under displacement control, the dislocation density is likely to be similar for a given applied strain, and hence overall, the stress responses for Ti-6242 are lower than those for Ti-6246 but without larger flow stress spacing with applied strain rate when compared with the Ti-6246 response in Fig. 5. However, under stress-controlled loading relevant to dwell conditions, the overall strain for Ti-6242 increased from 0.011 at the beginning of the stress dwell to 0.046 at the dwell end, while for Ti-6246, it increased from 0.002 to 0.003 during the stress dwell period which is very significantly lower. This is because under stress control, more slip occurs in the relatively 'soft' Ti-6242 alloy, and as a result, the dislocation density is higher, i.e. greater than 500 μm^{-2} compared to the 10 μm^{-2} observed for the Ti-6246 at the end of stress dwell.

4. Conclusions

A dislocation-based crystal plasticity approach has been utilised to extract thermal activation energies for pinned dislocation escape for the titanium alloys Ti-6242 and Ti-6246 (9.8×10^{-20} J and 10.6×10^{-20} J respectively) such that the remarkably different cold creep responses resulting from the inclusion of a stress dwell within the fatigue loading cycle are captured accurately. The model demonstrates that this behaviour is entirely consistent with that for strain-controlled loading without a stress hold for which the rate-sensitive responses of the two alloys are near-identical, entirely reflecting experimental observation.

A discrete dislocation model which explicitly includes the thermally activated escape of pinned dislocations and which utilises the activation energies obtained from crystal plasticity modelling has been presented and shown to predict the experimentally observed rate sensitivities of nano-indentation into basal and prism planes of alloys Ti-6242 and Ti-6246. Ti-6242 is shown to have a strong crystallographic orientation-dependent indentation rate sensitivity whilst Ti-6246 does not, such that in the former alloy, a slip-system dependent rate sensitivity exists. These predicted observations are found to be in agreement with recently published experimental measurements from nano-indentation tests.

The discrete dislocation model incorporating thermally-activated dislocation escape predicts that in alloy Ti-6242, under conditions of stress dwell within the fatigue loading cycle, the load shedding, or stress redistribution, is remarkable, leading to the establishment of very high basal stresses on badly orientated grain combinations, potentially sufficiently high to cause facet nucleation. However, alloy Ti-6246, because of its differing activation energy for dislocation escape, shows negligible stress redistribution and hence load shedding, therefore negating the potential for facet nucleation. A mechanistic explanation has therefore been provided for the elusive question of why Ti-6242 does show dwell debit whereas alloy Ti-6246 does not, which has significant potential for helping to alleviate this important industrial problem.

It has been shown that the physical phenomenon of key importance with respect to load shedding in the alloys considered is that of the time constant associated with the process of thermally activated dislocation escape, but with respect to the time constant associated with the loading. If the former differs substantially from the latter, dwell debit is diminished, and this is the case for Ti-6246 in the loading rate regime relevant to in-service conditions. However, for Ti-6242, the former and latter coincide leading to substantial load shedding and dwell debit.

Acknowledgments

ZZ acknowledges the financial support by the Engineering and Physical Sciences Research Council for funding through the HexMat programme grant EP/K034332/1 and the China Scholarship Council (CSC). FPED wishes to acknowledge gratefully the provision of funding for his Royal Academy of Engineering/Rolls-Royce Research Chair and EPSRC (as above).

References

Agnihotri, P.K., Van der Giessen, E., 2015. On the rate sensitivity in discrete dislocation plasticity. Mech. Mater. 90, 37–46.
Anahid, M., Samal, M.K., Ghosh, S., 2011. Dwell fatigue crack nucleation model based on crystal plasticity finite element simulations of polycrystalline titanium alloys. J. Mech. Phys. Solids 59, 2157–2176.
Bache, M.R., 2003. A review of dwell sensitive fatigue in titanium alloys: the role of microstructure, texture and operating conditions. Int. J. Fatigue 25, 1079–1087.
Bache, M.R., Cope, M., Davies, H.M., Evans, W.J., Harrison, G., 1997. Dwell sensitive fatigue in a near alpha titanium alloy at ambient temperature. Int. J. Fatigue 19, 83–88.
Balint, D.S., Deshpande, V.S., Needleman, A., Van der Giessen, E., 2006. Discrete dislocation plasticity analysis of the wedge indentation of films. J. Mech. Phys. Solids 54, 2281–2303.
Britton, T.B., Dunne, F.P.E., Wilkinson, A.J., 2015. On the mechanistic basis of deformation at the microscale in hexagonal close-packed metals. Proc. R. Soc. Lond. A: Math., 471.
Cottrell, A.H., Dexter, D., 1954. Dislocations and plastic flow in crystals. Am. J. Phys. 22, 242–243.
Dunne, F.P.E., Rugg, D., 2008. On the mechanisms of fatigue facet nucleation in titanium alloys. Fatigue Fract. Eng. Mater. Struct. 31, 949–958.
Dunne, F.P.E., Rugg, D., Walker, A., 2007a. Lengthscale-dependent, elastically anisotropic, physically-based hcp crystal plasticity: Application to cold-dwell fatigue in Ti alloys. Int. J. Plast. 23, 1061–1083.
Dunne, F.P.E., Walker, A., Rugg, D., 2007b. A systematic study of hcp crystal orientation and morphology effects in polycrystal deformation and fatigue. Proc. R. Soc. Lond. A: Math. 463, 1467–1489.
Evans, W.J., Bache, M.R., 1994. Dwell-sensitive fatigue under biaxial loads in the near-alpha titanium alloy IMI685. Int. J. Fatigue 16, 443–452.
Gerland, M., Lefranc, P., Doquet, V., Sarrazin-Baudoux, C., 2009. Deformation and damage mechanisms in an α/β 6242 Ti alloy in fatigue, dwell-fatigue and creep at room temperature. Influence of internal hydrogen. Mater. Sci. Eng.: A 507, 132–143.
Gibbs, G.B., 1969. Thermodynamic analysis of dislocation glide controlled by dispersed local obstacles. Mater. Sci. Eng. 4, 313–328.
Gong, J., Wilkinson, A.J., 2009. Anisotropy in the plastic flow properties of single-crystal α titanium determined from micro-cantilever beams. Acta Mater. 57, 5693–5705.
Gong, J., Wilkinson, A.J., 2011. A microcantilever investigation of size effect, solid-solution strengthening and second-phase strengthening for 〈a〉 prism slip in alpha-Ti. Acta Mater. 59, 5970–5981.
Hasija, V., Ghosh, S., Mills, M.J., Joseph, D.S., 2003. Deformation and creep modeling in polycrystalline Ti–6Al alloys. Acta Mater. 51, 4533–4549.
Jiang, J., Zhang, T., Dunne, F.P.E., Britton, T.B., 2016. Deformation compatibility in a single crystalline Ni superalloy. Proc. R. Soc. Lond. A: Math., 472.
Jun, T.-S., Armstrong, D.E.J., Britton, T.B., 2016a. A nanoindentation investigation of local strain rate sensitivity in dual-phase Ti alloys. J. Alloy. Compd. 672, 282–291.
Jun, T.-S., Sernicola, G., Dunne, F.P.E., Britton, T.B., 2016b. Local deformation mechanisms of two-phase Ti alloy. Mater. Sci. Eng.: A 649, 39–47.
Jun, T.-S., Zhang, Z., Sernicola, G., Dunne, F.P.E., Britton, T.B., 2016c. Local strain rate sensitivity of single α phase within a dual-phase Ti alloy. Acta Mater. 107, 298–309.
Kirane, K., Ghosh, S., 2008. A cold dwell fatigue crack nucleation criterion for polycrystalline Ti-6242 using grain-level crystal plasticity FE Model. Int. J. Fatigue 30, 2127–2139.
Lefranc, P., Doquet, V., Gerland, M., Sarrazin-Baudoux, C., 2008. Nucleation of cracks from shear-induced cavities in an α/β titanium alloy in fatigue, room-temperature creep and dwell-fatigue. Acta Mater. 56, 4450–4457.
Lütjering, G., Williams, J.C., 2003. In: TitaniumSpringer.
Mayo, M.J., Nix, W.D., 1988. A micro-indentation study of superplasticity in Pb, Sn, and Sn-38 wt% Pb. Acta Metall. 36, 2183–2192.
Neeraj, T., Hou, D.H., Daehn, G.S., Mills, M.J., 2000. Phenomenological and microstructural analysis of room temperature creep in titanium alloys. Acta Mater. 48, 1225–1238.
Ozturk, D., Shahba, A., Ghosh, S., 2016. Crystal plasticity FE study of the effect of thermo-mechanical loading on fatigue crack nucleation in titanium alloys. Fatigue Fract. Eng. Mater. Struct..
Pilchak, A.L., 2013. Fatigue crack growth rates in alpha titanium: Faceted vs. striation growth. Scr. Mater. 68, 277–280.
Pilchak, A.L., 2014. A simple model to account for the role of microtexture on fatigue and dwell fatigue lifetimes of titanium alloys. Scr. Mater. 74, 68–71.
Pilchak, A.L., Williams, J.C., 2010. Observations of facet formation in near-α titanium and comments on the role of hydrogen. Met. Mat. Trans. A 42, 1000–1027.
Qiu, J., Ma, Y., Lei, J., Liu, Y., Huang, A., Rugg, D., Yang, R., 2014. A comparative study on dwell fatigue of Ti–6Al–2Sn–4Zr–xMo ($x=2$ to 6) Alloys on a Microstructure-Normalized Basis. Met. Mater. Trans. A 45, 6075–6087.
Sinha, V., Mills, M.J., Williams, J.C., Spowart, J.E., 2006. Observations on the faceted initiation site in the dwell-fatigue tested ti-6242 alloy: Crystallographic orientation and size effects. Met. Mater. Trans. A 37, 1507–1518.
Stroh, A.N., 1954. The formation of cracks as a result of plastic flow. Proc. R. Soc. Lond. A: Math. 223, 404–414.
Suri, S., Viswanathan, G.B., Neeraj, T., Hou, D.H., Mills, M.J., 1999. Room temperature deformation and mechanisms of slip transmission in oriented single-colony crystals of an α/β titanium alloy. Acta Mater. 47, 1019–1034.
Van der Giessen, E., Needleman, A., 1995. Discrete dislocation plasticity: a simple planar model. Model. Simul. Mater. Sci. Eng. 3, 689.
Williams, J.C., Starke Jr, E.A., 2003. Progress in structural materials for aerospace systems. Acta Mater. 51, 5775–5799.
Zhang, Z., Cuddihy, M.A., Dunne, F.P.E., 2015. On rate-dependent polycrystal deformation: the temperature sensitivity of cold dwell fatigue. Proc. R. Soc. Lond. A: Math., 471.
Zhang, Z., Jun, T.-S., Britton, T.B., Dunne, F.P.E., 2016a. Intrinsic anisotropy of strain rate sensitivity in single crystal alpha titanium. Acta Mater. Rev..
Zhang, Z., Jun, T.-S., Britton, T.B., Dunne, F.P.E., 2016b. Rate-sensitive behaviour of alpha-beta colony Ti. Acta Mater. Rev..
Zheng, Z., Balint, D.S., Dunne, F.P.E., 2016. Rate sensitivity in discrete dislocation plasticity in hexagonal close-packed crystals. Acta Mater. 107, 17–26.
Zhu, H.X., Zhang, P., Balint, D., Thorpe, S.M., Elliott, J.A., Windle, A.H., Lin, J., 2014. The effects of regularity on the geometrical properties of Voronoi tessellations. Physica A: Stat. Mech. Appl. 406, 42–58.